

## Article

# Yield Adjustment Using GPR-Derived Spatial Covariance Structure in Cassava Field: A Preliminary Investigation

Afolabi Agbona <sup>1,\*</sup>, Osvaal A. Montesinos-Lopez <sup>2</sup>, Mark E. Everett <sup>3</sup>, Henry Ruiz-Guzman <sup>4</sup> and Dirk B. Hays <sup>1,4</sup><sup>1</sup> Molecular & Environmental Plant Sciences, Texas A&M University, College Station, TX 77843, USA<sup>2</sup> Facultad de Telemática, Universidad de Colima, Colima 28040, Mexico<sup>3</sup> Department of Geology & Geophysics, Texas A&M University, College Station, TX 77843, USA<sup>4</sup> Department of Soil and Crop Sciences, Texas A&M University, College Station, TX 77843, USA

\* Correspondence: aafolabi@tamu.edu

**Abstract:** Many processes concerning below-ground plant performance are not fully understood, such as spatial and temporal dynamics and their relation to environmental factors. Accounting for these spatial patterns is very important as they may be used to adjust for the estimation of cassava fresh root yield masked by field heterogeneity. The yield of cassava is an important characteristic that every breeder seeks to maintain in their germplasm. Ground-Penetrating Radar (GPR) has proven to be an effective tool for studying the below-ground characteristics of developing plants, but it has not yet been explored with respect to its utility in normalizing spatial heterogeneity in agricultural field experiments. In this study, the use of GPR for this purpose was evaluated in a cassava field trial conducted in Momil, Colombia. Using the signal amplitude of the GPR radargram from each field plot, we constructed a spatial plot error structure using the variance of the signal amplitude and developed GPR-based autoregressive (AR) models for fresh root yield adjustment. The comparison of the models was based on the average standard error (SE) of the Best Linear Unbiased Estimator (BLUE) and through majority voting (MV) with respect to the SE of the genotype across the models. Our results show that the GPR-based AR model outperformed the other models, yielding an SE of 9.57 and an MV score of 88.33%, while the AR1 × AR1 and IID models had SEs of 10.15 and 10.56% and MV scores of 17.37 and 0.00%, respectively. Our results suggest that GPR can serve a dual purpose in non-destructive yield estimation and field spatial heterogeneity normalization in global root and tuber crop programs, presenting a great potential for adoption in many applications.

**Keywords:** ground-penetrating radar; cassava; heterogeneity; amplitude; variance; spatial; fresh yield



**Citation:** Agbona, A.; Montesinos-Lopez, O.A.; Everett, M.E.; Ruiz-Guzman, H.; Hays, D.B. Yield Adjustment Using GPR-Derived Spatial Covariance Structure in Cassava Field: A Preliminary Investigation. *Remote Sens.* **2023**, *15*, 1771. <https://doi.org/10.3390/rs15071771>

Academic Editors: Huajun Tang, Wenbin Wu and Wenjuan Li

Received: 24 February 2023

Revised: 17 March 2023

Accepted: 22 March 2023

Published: 25 March 2023



**Copyright:** © 2023 by the authors. Licensee MDPI, Basel, Switzerland. This article is an open access article distributed under the terms and conditions of the Creative Commons Attribution (CC BY) license (<https://creativecommons.org/licenses/by/4.0/>).

## 1. Introduction

Proximal sensing is increasingly expanding its impact on a wide variety of agricultural applications [1,2]. The field of proximal sensing has rapidly evolved alongside advances in sensor technologies, thus easing its adoption and deployment. Cassava (*Manihot esculenta* Cranz) is the least expensive abundant source of carbohydrates, delivering higher amounts of starch per unit area compared to other staple crops [3]. Producing cassava requires only modest inputs and affords farmers great flexibility in terms of the timing of the harvest, as this crop can be left in the ground even after reaching physiological maturity [4]. The yield of cassava is an important characteristic that every breeder seeks to maintain in their germplasm. A high-yielding cultivar can serve a dual purpose for the farmer, constituting a source of income and food for the family. In addition, farmers also want a cultivar that matures early [5]. For many years, a morphological or visual system that allows breeders to recognize when a cassava plant starts to bulk or mature has been unavailable. However, following the advent of the application of ground-penetrating radar (GPR) to the field of agriculture, this is now possible [6,7].

In breeding experiments, the estimation of the true genetic value of the variables of interest, such as yield, early maturity, etc., for these cultivars is of great importance.

However, errors due to field heterogeneity often mask this estimation. A common approach used to mitigate the problem of field heterogeneity is the use of an efficient experimental design through blocking, a term that describes the grouping of experimental units; a block is also known as an experimental plot [8]. Blocking is considered to be efficient based on the assumption that the variation within a block is smaller compared to the variation between blocks; however, in practice, this assumption does not often hold if the block size is large.

Nearest Neighbor (NN) and related statistical methods have been developed and used to account for spatial dependency in the field [9–12]. Of all the NN variants, the one proposed by Gilmour et al. (1997) [12] has been widely used in agricultural experiments in which neighboring experimental plots are equidistant from each other. The method uses the first-order, separable autoregressive structure (AR) of residuals as a direct product of row and column functions ( $AR1 \times AR1$ ). Hence, row- and column-based information is important for modelling spatial dependency. Accounting for spatial dependency helps to improve yield estimation and predictions that are potentially masked by field heterogeneity.

Laboratory analyses of soil samples from experimental plots have also been used to discern field heterogeneity based on carefully measured soil properties [13–15]; however, such analyses are costly. Soil probes and other in situ tools have also been used to characterize important soil parameters [16–19]; in some cases, the outputs of these probes are imported into an established empirical equation to derive the desired soil parameter. GPR, a type of proximal sensing, has been used to study the spatial variability of soil moisture content at the field scale based on calculated ground wave velocity, soil permittivity, and empirically estimated volumetric moisture content [20–24]. Soil organic carbon content of different soil layers has also been estimated in conjunction with additional secondary covariates from electromagnetic induction (EMI) surveys [25].

To the best of our knowledge, the present work is the first investigation in the field of agriculture to use multi-channel GPR for assessing and adjusting for spatial variation in yield. The quantification of soil heterogeneity developed in this study is an extension of the variance of amplitude method described by Fedorova et al. [26]. GPR has established itself in several disciplines, such as geoscience, civil engineering [27,28], archeology, the military [29], and the study of forest ecosystems [30,31]. It is increasingly being applied in agriculture for the estimation and prediction of root biomass [6,7,32–34]. However, the adoption of GPR into agriculture should increase if its multipurpose utility is further explored.

Accordingly, the objectives of this study were as follows:

- (a) Plan and execute an experimental design based on a multi-antenna GPR array;
- (b) Evaluate the ability of GPR to account for spatial variation at the field scale;
- (c) Evaluate the improvement in yield estimation after adjustment for GPR-derived spatial variation.

## 2. Materials and Methods

### 2.1. Ground-Penetrating Radar (GPR)

GPR is a geophysical tool used for exploring the subsurface of the earth to depths ranging from several cm up to several km under ideal conditions [35]. It consists of a transmitter emitting a pulse of electromagnetic energy (EME) along with a receiver that records any subsurface reflections. Changes in relative dielectric permittivity of the geological medium through which the wave propagates often cause reflections. GPR measures both the amplitude and the travel time of the reflected energy [36]. The GPR system used in this study (Figure 1) is an experimental prototype system developed by IDS Georadar from Pisa, Italy.

The system is composed of a transmitter and receiver, an antenna array, and a mobile computer. The apparatus is cart-mounted for maneuverability in both regular and irregular terrain. The computer controls the manufacturer-supplied software for data acquisition and display. The antenna array is an air-launched bistatic configuration (see Table 1) of a modified vee-dipole, wideband frequency of 1.8 GHz, and vertically polarized antennas [37,38].

The array comprises 8 identical antennas spaced 0.04 m apart with user-defined pairing of transmitting and receiving antennae [6]. The data visualization modes are presented in Figure 2.

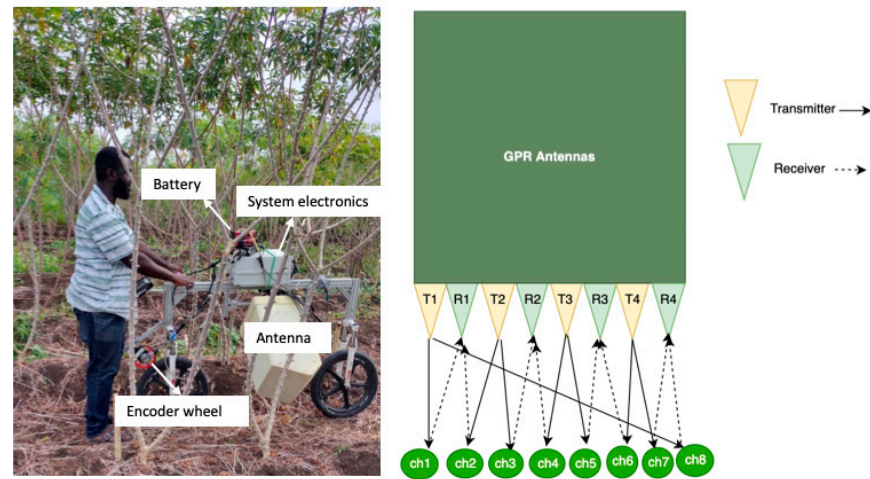


**Figure 1.** (Left) GPR device; (right) antenna configuration showing 8 channels of antenna pairing.

**Table 1.** Data acquisition parameters.

	Field Measurement Input Parameter	Value
1	Frequency range (est.)	1.3–2.3 GHz
2	Central frequency	1.8 GHz
3	Effective depth penetration	~0.8 m
4	Spatial resolution	0.01 m
5	Number of samples	512
6	Temporal resolution	18 ns
7	Antenna spacing	0.04 m

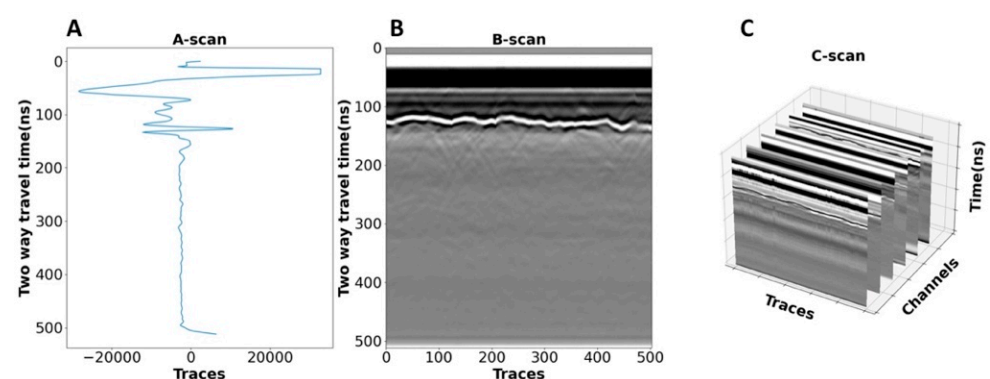


**Figure 2.** GPR radargram visualization: (A) A-scan representing the signal received via a single outgoing pulse at a given transmission–reception antenna’s location; (B) B-scan representing the series of A-scan pulses from a single antenna transect; and (C) C-scan representing collection of B-scans. Adapted from [6].

## 2.2. Field Trial

This study was conducted during a field trial at the International Center of Tropical Agriculture (CIAT), Momil, Colombia, in 2021. One hundred and ninety (190) genotypes were planted in two field replications (each genotype is present in two field plots), which were laid out in nineteen rows (herein referred to as field rows) and twenty columns;

consequently, three hundred and eighty (380) agricultural field plots (see Figure 3) were scanned using GPR to quantify the soil heterogeneity within each plot. A single plot corresponds to dimensions of  $3.5 \text{ m} \times 2.6 \text{ m}$  and comprises 2 rows (herein referred to as plot rows) of 5 plant stands. The within-plot and between-plot row spacing is 0.7 m and 1.0 m, respectively. Only the inner 6 plants (a net plot consisting of 2 rows of 3 plants) were scanned by GPR. The outermost plants were excluded due to the possibility of edge effects (this is a common practice in agricultural experiments whereby the inner plant stands are shielded from environmental and physical stress by the outermost plants). A plot row is hemispherical in shape, and overall, the field comprises a regular grid with nearest-neighbor plots equidistant at 1.0 m.

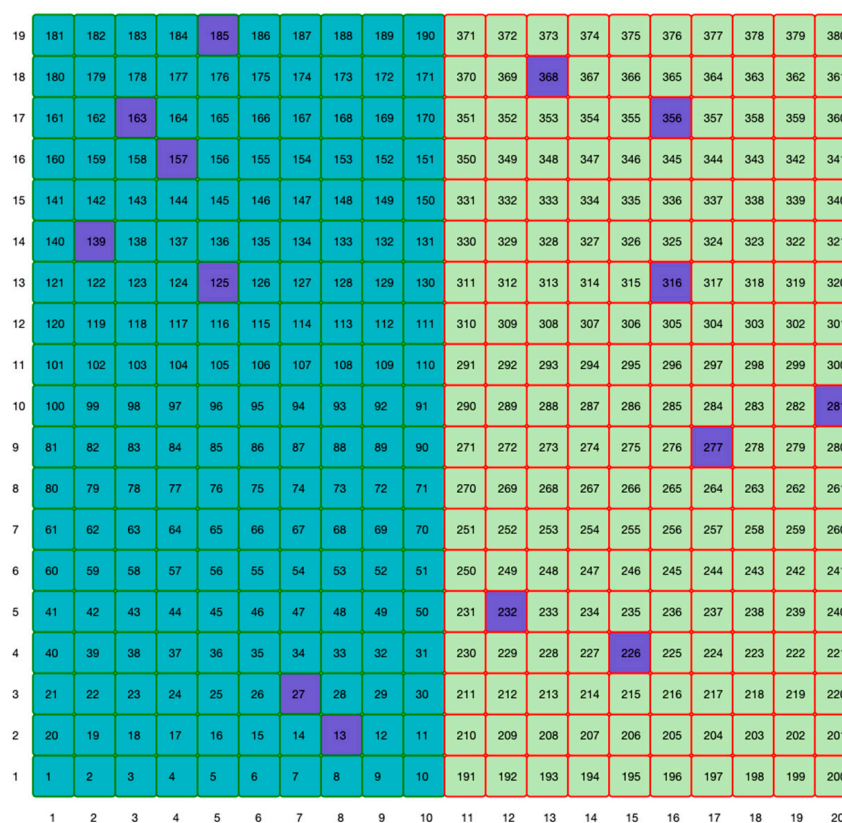


**Figure 3.** Field Map. The purple shading indicates the location of the experimental checks (control cultivars). The teal and olive colors show the different replications. The X and Y axis correspond to the field column (longitude) and field row (latitude), respectively, and are used to reference the field plot.

### 2.3. Radar Acquisition Device

The plot rows were scanned in both directions (as illustrated in Figure 4). The cart carrying the GPR antenna array was pulled at constant speed, with the antennas tilted toward the plot's interior at a  $\sim 0.5 \text{ m}$  standoff and an inclination of  $135^\circ$  with respect to the surface of the ground.

Each plot is represented by 4 B-scans (Row1E and W; Row2E and W (see Figure 5)). A total of 1520 ( $380 \text{ plots} \times 2 \text{ transects} \times 2 \text{ plot rows}$ ) GPR profiles were collected. Variance of amplitude (VOA) (see Equation (1) below) was calculated and summed across all the B-scans. After GPR scanning was completed, fresh root yield (the ground-reference data, hereinafter referred to as 'fyld') of harvested cassava (bulked together from the 6 plant stands) was measured in kilogram per plot using a weighing pan and suspended salter scale.

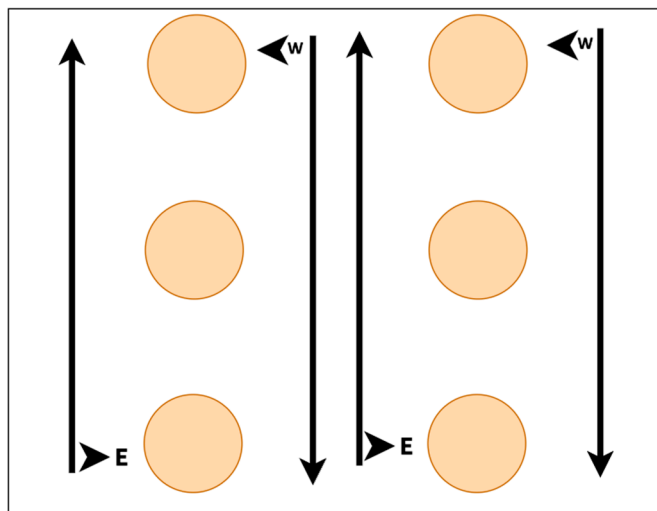


Figure 4. Plot rows showing direction of transect.

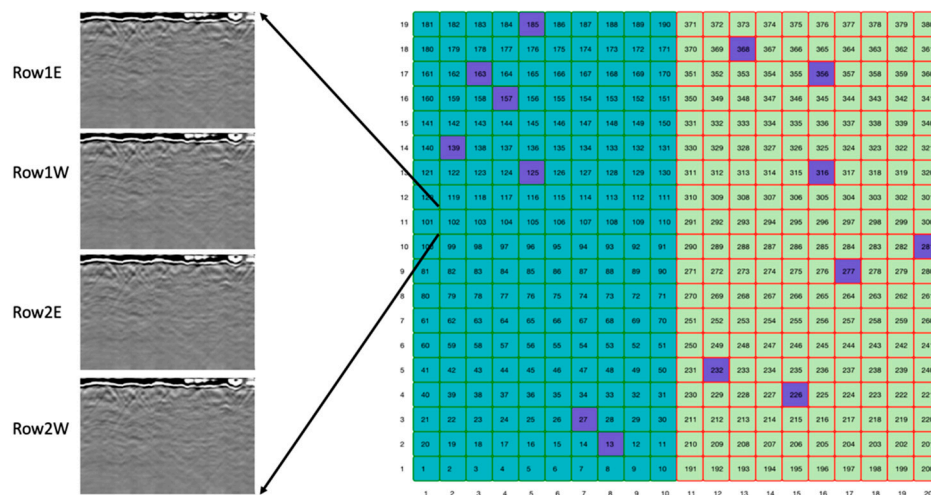


Figure 5. Sample field plot representation using 8-bit gray-scale B-scan (left).

Variance of amplitude (VOA) of each radar signal trace in each transect from a representative TX–RX antenna pair (only channel 8 is used in this paper) is calculated as described in the following equation [26]:

$$\text{Var}(X) = \sum_{i=T_1}^{T_n} \frac{(X_i - \bar{X})^2}{n} \tag{1}$$

where  $X_i$  is a vector containing the amplitudes of each sample of the  $i$ -th trace;  $\bar{X}$  is a vector containing the mean value of the signal amplitude of the  $i$ -th trace;  $T_1 \dots T_n$  is the time interval of each trace; and  $n$  is the number of samples in a trace. The mean of the calculated variances of each trace ( $\text{Var}(X)$ ) is then computed across all traces in a transect.

Before VOA is calculated, a background correction is applied to the radargrams to mitigate coherent sub-horizontal reflected energy; then, each GPR vertical section of the radargram is carefully inspected and trimmed from the ground surface to a depth where the signal amplitude level is just above the noise floor. The noise floor is the amplitude level below which a signal can no longer be visually discerned.

Changes in variance of the signal amplitude are expected to be related to changes in the number of radar-reflective boundaries within the soil medium; thus, they should provide a proxy measure of heterogeneity. In total, there are 380 VOA and fyld determinations, that is, one for each field plot. GPR-derived VOA is used in this manner to



investigate spatial dependency across the field plots and adjust for measured field. GPR data processing and estimation of VOA was performed using GPR-Studio version 2.0, a web-based application [39].

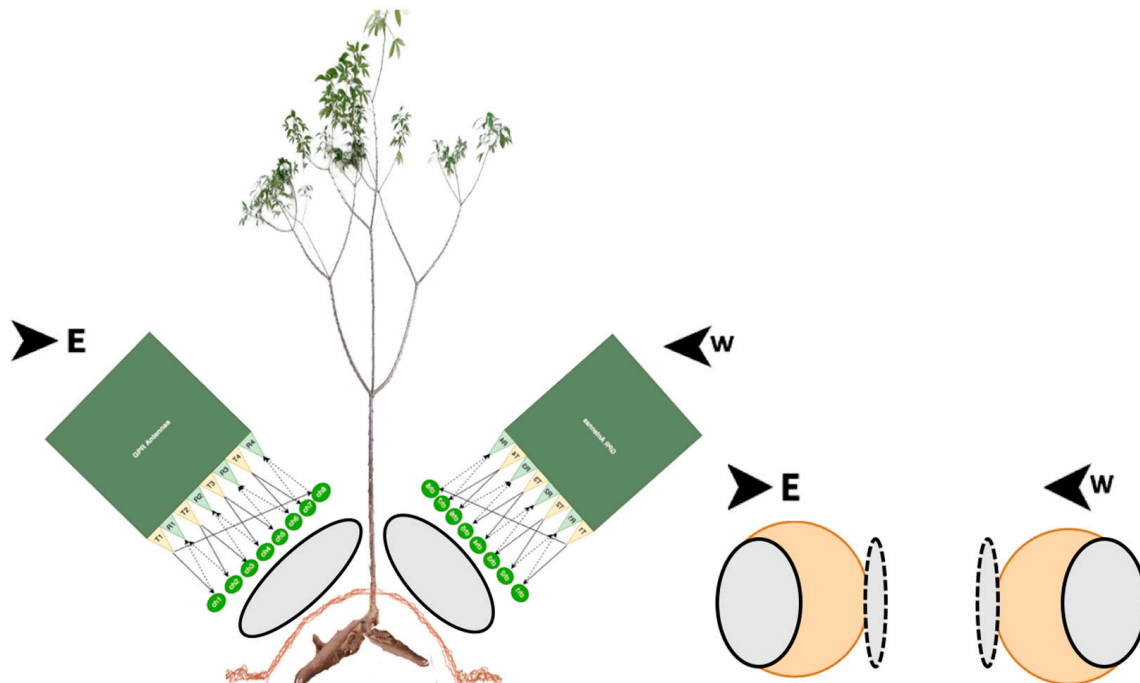
#### 2.4. Sampling Strategy and Fresnel Zone Footprint

From the five available rows, only the inner rows (2, 3, and 4) were scanned using GPR. The Fresnel zone footprint illuminated by the GPR antenna array is the area of ground, at a given depth, from which detectable return signals are recorded. The footprint is herein conceptualized as the cross-section of an elliptical cone whose apex is at the TX antenna and whose major axis  $D$  at some vertical offset  $h$  from the antenna is estimated using the following formula [24,40]:

$$D = \sqrt{\frac{\lambda^2}{4} + 2\lambda h} \quad (2)$$

where  $\lambda$  is the wavelength at the central frequency of the antenna in free space. A vertical offset of  $h = 0.5$  m is used to calculate  $D$ , which is an average of 0.4 m and 0.6 m in vertical height at both ends of the array. Thus, we are calculating the size of the footprint at the ground surface.

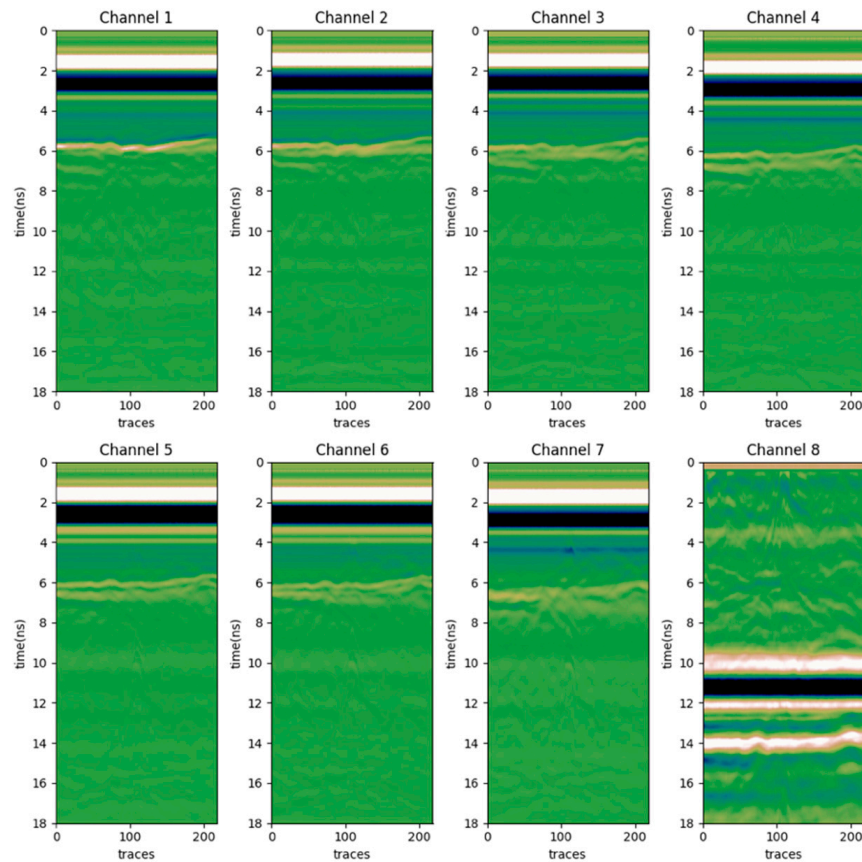
The Fresnel zone footprint of our GPR apparatus has a major axis of  $D \sim 0.42$  m, thereby illuminating  $\sim 60\%$  of each side of a hemispherical plot row (the entire width of the plot row is  $\sim 0.7$  m). Thus, the area of ground scanned using GPR extends to the other side of a row during each transect (Figure 6). Considering the 0.04 m spacing between the 8 TX–RX channels, each channel thus contributes  $\sim 0.02$  m to the entire footprint. Based on the angle of inclination in each transect, the length of the side of the ridge on the hemispherical plot row ( $\sim 0.4$  m) is compared to  $D$  ( $\sim 0.42$  m); radar signal return from channel 8 is assumed to originate from the other side of the plot row without roots. Hence, information from channel 8 is used to characterize the host soil medium.



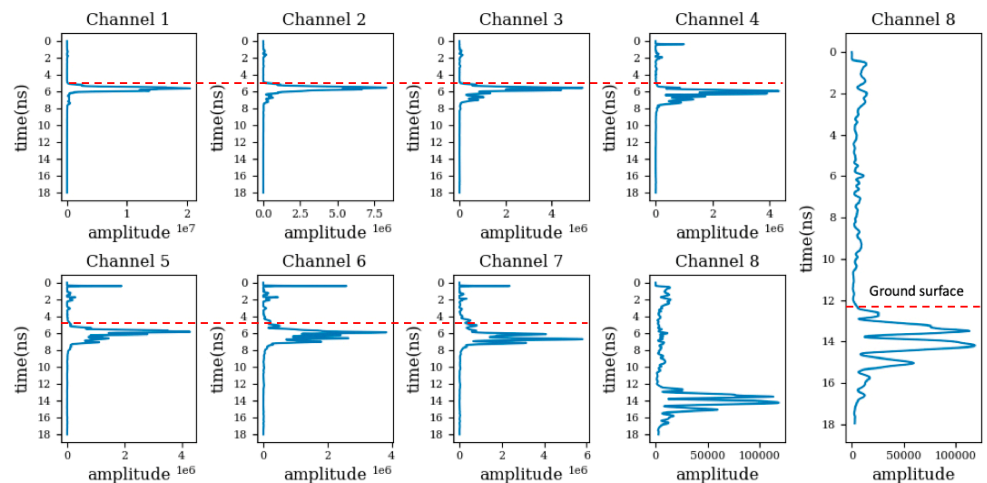
**Figure 6.** Fresnel zone on sample ridge on a plot row (left). The footprint is extended to the other side of the ridge in each transect (right).

Figure 7 shows raw radargrams from all 8 TX–RX channels along a representative transect. Figure 8 depicts the average radar signal amplitudes on each channel and their summation across the channels. It is evident that the radar signal on channel 8 is offset in

time and shows a strikingly lower maximum amplitude ( $\sim 10^6$ , arbitrary units) compared to the other channels (amplitude  $\sim 10^7$ ).



**Figure 7.** Radargrams from all 8 channels. Observed time delay in channels 1 to 7 is approximately uniform, while there is a consistent, excessive time delay observed in channel 8, which might be due to some element of ground-wave arrival in the path of its antenna pair.



**Figure 8.** Distribution of amplitude across the 8 channels after background correction was applied. The red dashed line indicates the ground surface in each channel. The peaks below the ground surface in channels 1 to 7 are mostly reflections from cassava root, while those of channel 8 are from host soil medium.

## 2.5. Test for Spatial Dependency

### 2.5.1. Spatial Neighborhood Matrices

In order to test if there is spatial correlation amongst the GPR-derived VOA values of the field plots, the spatial neighborhood must be defined. The concept of spatial contiguity across a wide area is useful for understanding a localized or “neighborhood” structure. The field row ( $i$ ) and column ( $j$ ) are used as the spatial coordinates (Figure 3); hence, they can be used to calculate a spatial weight based on the Euclidean distance between plots on field location ( $i, j$ ). The ( $i, j$ )th element of a spatial neighborhood matrix  $W$ , denoted by  $W_{ij}$ , describes the spatial relationship between row  $i$  and column  $j$ , which defines a neighborhood structure over the field (Figure 9 and Table 2). The elements of  $W$  are regarded as the spatial weights. A larger weight is associated with columns that are closer to a given row  $i$  than those farther away. In this study, a distance threshold of 1.2 m is set, wherein two points farther apart than the threshold are not considered to be neighbors. A binary, sparse adjacency matrix is constructed such that  $W_{ij} = 1$  if locations  $i$  and  $j$  share a common boundary; otherwise,  $W_{ij} = 0$  and is used for subsequent autoregressive modeling (described in Section 2.6).

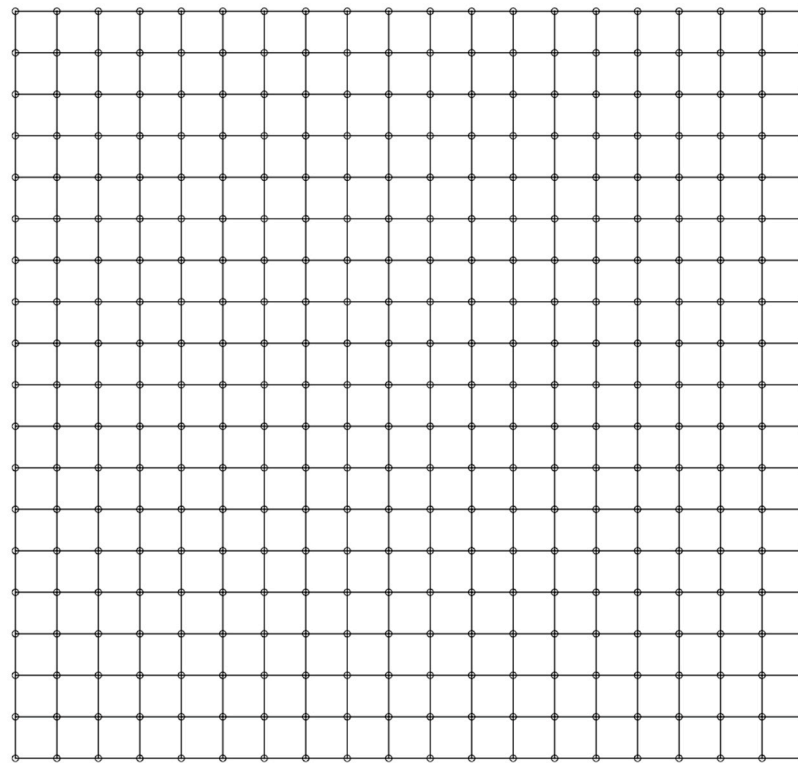


**Figure 9.** Neighborhood structure. It shows a global structure wherein most plots are connected.

**Table 2.** Spatial neighborhood information.

Neighborhood Parameter	Value
Number of regions	380
Number of non-zero links	1822
Percentage of non-zero weights	1.26
Average number of links	4.80

### 2.5.2. Global Moran’s I Statistic

Moran’s  $I$  statistic (Moran’s  $I$ ) is commonly used in spatial statistics to assess global spatial autocorrelation. Herein, it is used to estimate correlations of the GPR-derived



VOA between neighboring plots and, subsequently, find patterns [41]. In terms of its interpretation, Moran's  $I$  is similar to the Pearson correlation coefficient, with values  $-1 \leq I \leq 1$  ranging from a strong negative relationship between two variables to a strong positive relationship. The value  $I = 0$  suggests no spatial relationship between the variables. An estimated Moran's  $I \sim 0.77$  supports a hypothesis that the spatial distribution of VOA is not random but instead forms clusters in space. The 'lm.morantest' function of the 'spdep' R package [42] was used to estimate Moran's  $I$  based on Equation (3) below

$$I = \frac{N \sum_{i=1} \sum_{j=1} W_{ij} (x_i - \bar{x})(x_j - \bar{x})}{K \sum_{j=1} (x_i - \bar{x})^2} \quad (3)$$

where  $N$  is the number of field plots;  $W_{ij}$  is the element in the spatial weight matrix corresponding to the pair defined by row  $i$  and column  $j$ ;  $x_i$  and  $x_j$  are the GPR-based observations (of VOA) at specific locations  $i$  and  $j$  in the field plot;  $\bar{x}$  is the grand mean value of VOA across all locations in the field plot; and  $K = \sum_i \sum_j W_{ij}$  is the sum of all matrix elements.

## 2.6. Spatial Process Model

In this section, autoregressive models are fitted and compared for the purpose of creating a VOA covariance matrix, which is then used as a custom or user-defined plot error structure for  $\text{fyld}$  adjustment. Consider a model in which observations in neighboring locations are more similar to each other than observations that are farther apart; such a model contains a component of random smoothing according to the neighborhood structure and an unstructured component that models uncorrelated noise [43].

Simultaneous (SAR) and conditional autoregressive (CAR) models (as shown in Equations (4)–(7), respectively) are used to model spatial dependency using the GPR-derived VOA as the response variable, and replication, field row, and column as covariates. Both SAR and CAR models were fitted using the 'spautolm' function of the R package 'spdep' [42]. In order to stabilize the variance in VOA, a natural logarithm transformation was applied; hence,  $\log\text{VOA}$  was used during modelling. A model that considers identical and independent (IID) variance along field rows and columns (Equation (8)) was used as the baseline model. The spatial covariance structure is revealed by the covariance matrices that are calculated as a result of the SAR and CAR modeling. The response variables are described in both cases by a Gaussian distribution (see Equations (5) and (7)).

$$y(s_i) = \rho \sum_{j=1}^n w_{ij} y(s_j) + \epsilon \quad (4)$$

$$y \sim \mathcal{N}(0, \sigma^2 ((1 - \rho W)^{-1}) ((1 - \rho W)^{-1})^T) \quad (5)$$

$$y(s_i) |_{-s_i} \sim \mathcal{N}\left(\rho \sum_{j=1}^n w_{ij} y(s_j), \sigma^2\right) \quad (6)$$

$$y \sim \mathcal{N}\left(0, \sigma^2 (1 - \rho W)^{-1}\right) \quad (7)$$

$$y = \mu + \text{row}_i + \text{col}_j + \epsilon_{ij} \quad (8)$$

In the previous equations,  $y = \log\text{VOA}$ ;  $W$  is a row-standardized spatial weight matrix (the standardization is achieved by dividing each neighbor's weight by the sum of all neighbors' weights);  $\rho$  is the spatial autoregressive coefficient, which can be regarded as the estimated spatial correlation ( $\rho$ );  $\sigma^2 ((1 - \rho W)^{-1}) ((1 - \rho W)^{-1})^T$  is the SAR model VOA-derived covariance matrix; and  $\sigma^2 (1 - \rho W)^{-1}$  is the CAR model VOA-derived covariance matrix. In addition,  $\mu$  is the intercept (overall mean), whereas  $\text{row}$  and  $\text{col}$  are normally

distributed (for which Equation (8) describes the baseline model) with constant variances ( $N(0, \sigma_{row}^2$  and  $N(0, \sigma_{col}^2)$ ).

### 2.7. Spatial Model for Yield Adjustment

In this section, the GPR-derived spatial covariance matrix (described in Section 2.6) is used to assess improvement in our model's estimation of fyld (the agronomic trait of interest) compared to other models. This trait was analyzed within a linear mixed-model framework; however, all effects were considered fixed (the model parameters are non-random quantities). Three univariate linear models were fitted; they differ in terms of their plot error structure ( $\epsilon$ ), and can be described as follows:

The first model (AR1  $\times$  AR1) considers the covariance matrix of the plot error structure ( $\sigma^2 \Sigma$ ) in the form of  $\Sigma_{col} \times \Sigma_{row}$  [12].  $\Sigma_{col}$  and  $\Sigma_{row}$  are  $20 \times 20$  and  $19 \times 19$  matrix functions of the column and row autoregressive parameters, respectively.

$$y_{pqkm} = \mu + gen_p + rep_q + row_{kq} + col_{mq} + \epsilon_{pqkm} \quad (9)$$

The second model (GPR-VOA) uses the VOA-derived covariance matrix (the GPR-derived spatial covariance structure as described previously in Equations (5) and (7)).

$$y_{pqkm} = \mu + gen_p + rep_q + row_{kq} + col_{mq} + \epsilon_{voa} \quad (10)$$

The third model considers constant variance along field rows and columns. This model is equivalent to the identical and independent (IID) model described in the previous section; however, the response variable modelled in this case is fyld.

$$y_{pqkm} = \mu + gen_p + rep_q + row_{kq} + col_{mq} + \epsilon_{pqkm} \quad (11)$$

In Equations (9)–(11),  $y_{pqkm}$  is the ( $380 \times 1$ ) vector of model-estimated fyld;  $\mu$  is the intercept (overall mean);  $gen_p$  is the genotype effect;  $rep_q$  is the effect of the replication  $q$ ;  $row_{kq}$  is the effect of row  $k$ 's interaction with replication  $q$ ;  $col_{mq}$  is the effect of column  $m$ 's interaction with replication  $q$ ;  $\epsilon_{pqkm}$  and  $\epsilon_{voa}$  are the residual terms (plot error structure), which are assumed to follow a Gaussian distribution;  $\epsilon \sim N(0, \sigma_{\epsilon}^2 \Sigma)$ ;  $\epsilon_{voa} \sim N(0, \sigma_{\epsilon_{voa}}^2 \Sigma)$ ; and  $\epsilon \sim N(0, \sigma_{\epsilon}^2 I)$  for Equations (9), (10) and (11) respectively.

The outcome of the model described in Equations (9)–(11) is an adjusted average fyld for each genotype. The outcome is regarded as the Best Linear Unbiased Estimator (BLUE). The adjustment is based on the explanatory variables, namely, genotype, replication, rows and columns (common to the three models), and plot error structure (different in each model). In order to compare the performance of the models, the standard error (SE) values of the BLUE of each genotype were obtained. The lower the SE, the better the model. Firstly, the overall average SE was compared between the models; secondly, a majority-voting (MV) procedure based on the individual SE of the genotype was carried out whereby the frequency of lower SE values when compared across the three models is expressed as a percentage [44]. The higher the percentage, the better the model, and vice versa. For example, consider the following procedure: obtain the SE of genotype "A" in each of the models; compare and record a count of when the SE in the GPR-VOA model is less than that of the AR1  $\times$  AR1 and IID models. Estimation of the parameters of Equations (9)–(11) was performed using the 'gls' and 'remlf90' functions in R packages 'nlme' [45] and 'breedR' [46].

### 2.8. Spatial Kriging

In this section, the possibility of minimizing time spent on GPR data acquisition in the field is evaluated by considering random sampling of GPR-derived VOA (variance of amplitude derived from the GPR radargram) in some field plots and then predicting VOA of the unsampled plots. The universal kriging interpolation method is considered for this approach. Kriging models consist of two parts, as shown in Equation (12) given

below. The first part is  $f(x)$ , which models the drift of the VOA mean. The second part is a random process,  $C(x)$ . The latter is a spatially autocorrelated error assumed to be a Gaussian stationary process [47]. The kriging procedure involves predicting VOA in an unsampled field plot by assuming that it has the form of a weighted average of the sampled VOA from spatially correlated field plots. The predictions are evaluated through spatial best unbiased linear prediction (BLUP), which is conditioned on the model covariance parameters. The latter include sill, nugget and range, prior distributions and MCMC (Markov Chain Monte Carlo) sampler starting values, and Metropolis proposal variance. The model parameters are described and implemented in the 'spLM' function in 'spBayes' R package [48]. A favorable prediction is an  $r$ -value that is close to 1. The kriging equations are as follows:

$$y = f(x) + C(x) \quad (12)$$

$$\hat{y}(x_0) = X^T(x_0)\beta + h^T(x_0)(C_{n,n} + \tau^2I)^{-1}(Y - X\beta) \quad (13)$$

where  $h(x_0) = (C(x_0, x_1), \dots, C(x_0, x_n))^T$ , i.e., the covariances of VOA between the sampled and unsampled field plots;  $\hat{y}(x_0)$  is the predicted VOA;  $C_{n,n}$  is the covariance among old locations;  $\tau^2$  denotes random residual variance;  $X$  represents the independent effect of replication; and  $\beta$  denotes the regression coefficient. All analysis was conducted using R software [49].

### 3. Results

#### 3.1. Spatial Distribution of VOA and FYLD

The spatial distribution of the VOA extracted from the GPR radargrams is shown in Figure 10. Separate boxplots are presented for VOA as a function of plot rows and columns. The boxplots indicate that there are significant complexities to the VOA distribution along both columns and rows. However, Figure 11 shows that plot heterogeneity based on the VOA proxy varies somewhat systematically across the field replications, whereas fyld shows a fairly random distribution. There is little or no spatial correlation (Pearson correlation  $r \sim 0.1$ ) between these variables (Figure S1). An explanation for this phenomenon is that fyld is expected to be influenced mainly by the genetic potential of the genotype rather than the GPR-sensed field heterogeneity.

#### 3.2. Spatial Model Comparison

The parameters extracted from the best-fitting spatial process model are presented in Table 3. The result shows that the CAR model has a higher spatial autoregressive coefficient, namely,  $\rho \sim 0.48$ , compared to the SAR model, whose value is  $\rho \sim 0.27$ . However, the model selection criteria such as the Corrected Akaike Information Criteria (AICC), which adjusts for the number of model parameters and observations, and the log likelihood [50] reveal almost no differences. The AICC and log likelihood values for the SAR model are  $-619.71$  and  $313.97$ , respectively, whereas they are  $-619.34$  and  $313.79$ , respectively, for the CAR model. The lower the AICC and the higher the log likelihood estimate, the more favorable the model [50]. Using the same criteria, the IID model (which assumes an identical and independent degree of residual variance) appears to have outperformed both the SAR and CAR models. IID has the lowest AICC ( $-627.73$ ) and the highest log likelihood estimate ( $317.98$ ). Conversely, the Moran's  $I$  test of spatial autocorrelation confirmed that there is spatial dependency ( $I = 0.77$ ) amongst the GPR-derived VOA measurements on the field plots. A consideration of the no-spatial-dependence model (IID) implies an assumption of spatial independence. Such an assumption may allow the field's actual spatial heterogeneity to mask the true fyld potential of each genotype. To this end, we determined that the CAR model was more favorable than the IID model. The CAR model assumes the spatial version of the Markov property; thus, the VOA of a plot is influenced by the neighboring plots. Whereas the SAR model assumes the "neighbors of neighbors" effect, i.e., the VOA of a plot is not only influenced by the neighboring plots but also by neighbors of those neighboring

plots [51]. Accordingly, the CAR-model-based VOA-derived plot error structure (refer to Equation (7)) should be used for fylld adjustment.

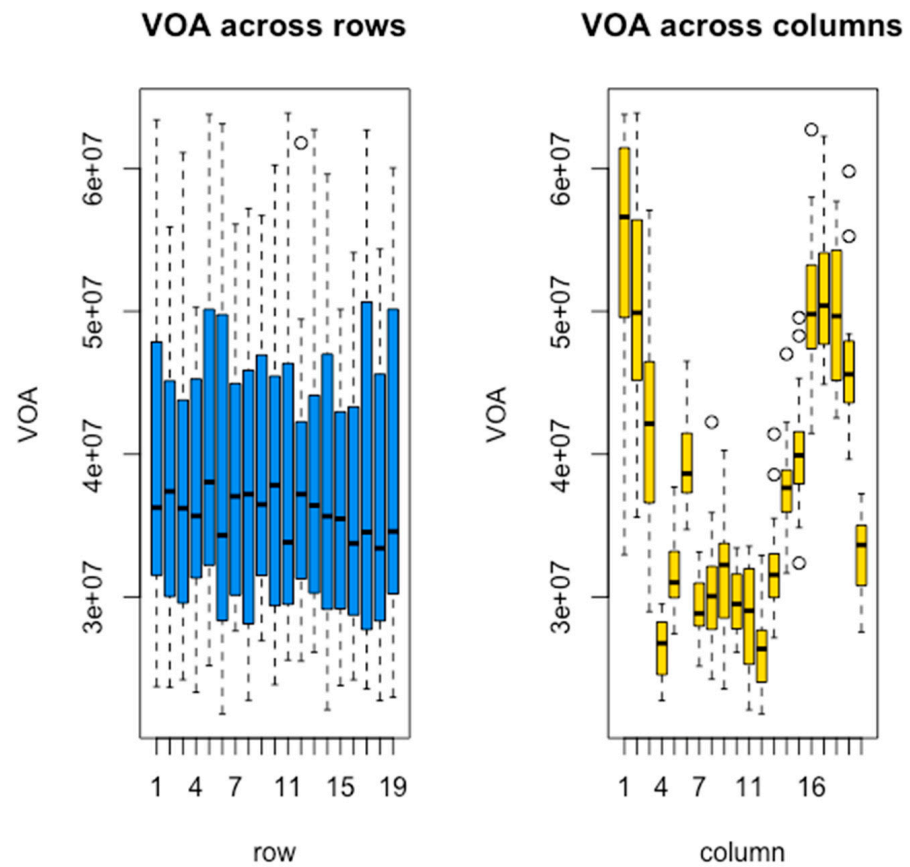


**Figure 10.** Boxplot showing the distribution of raw values of VOA across fields' rows and columns.

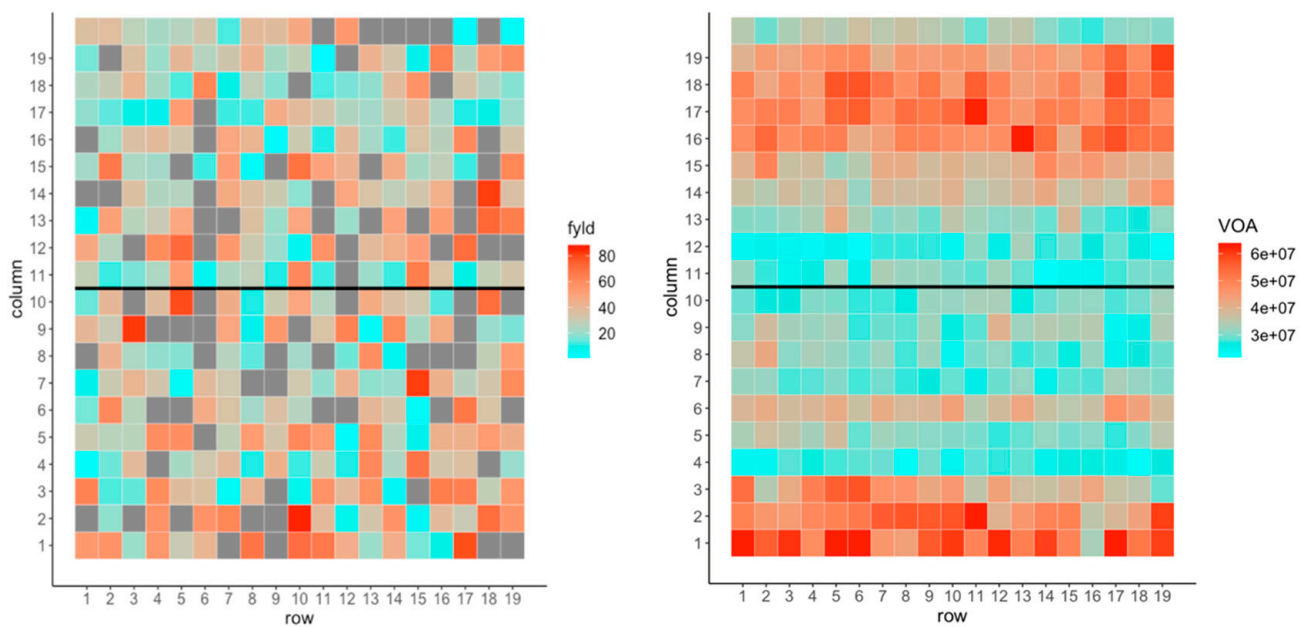


**Figure 11.** Heatmap showing the distribution of fylld (left) and the raw values of VOA (right) throughout replications.

**Table 3.** A table comparing SAR, CAR, and IID (no spatial) models.

	SAR	CAR	IID
Intercept	17.47	17.43	17.37
rho	0.27	0.48	N/A
Sigma <sup>2</sup>	0.01	0.01	0.07
Log likelihood	313.97	313.79	317.98
AICC	−619.71	−619.34	−627.73

### 3.3. Adjusting Estimation of Fyld Using VOA-Defined Covariance Structure

The results presented in Table 4 show that the GPR-VOA model that uses the VOA plot error structure has a slightly lower average standard error (SE) of the BLUE and a higher majority voting (MV) score compared to the model that uses the AR1 × AR1 plot error structure and the IID model. However, the differences are subtle in terms of SE but highly contrasting with respect to MV when compared with the AR1 × AR1 model, and they exhibit a great degree of disparity when compared to the IID model. Since the BLUE is an adjusted average of fyld using genotype, replication, row and column (common to the three models), and plot error structures (different in each model), a lower average SE suggests the superior accuracy of the estimated fyld. The same principle applies to MV that considers SE on a genotype-by-model level (the frequency of low occurrences is reported in percentages; hence, a higher value is better). Consequently, using the GPR-derived VOA plot error structure, a phenomenon referred to as a custom error covariance structure in the statistical paradigms thus helps improve the degree of adjustment to fyld estimation, as the inherent field variation is captured to some degree by the GPR measurements.

**Table 4.** Model comparison using AICC, average standard error (avgSE) of BLUE, and majority voting. Overall average of the BLUE is presented as avgBLUE.

Model	avgBLUE	AICC	avgSE	Majority Voting (MV)
GPR-VOA	27.09	−17,911.01	9.57	88.33
AR1 × AR1	22.23	−932.48	10.15	10.56
GPR-VOA	27.09	−17,911.01	9.57	100
IID	21.81	−378.99	17.37	0

### 3.4. Prediction in Untested Locations

The prediction of VOA in field locations where GPR surveys were not conducted was tested using the universal kriging interpolation method. This approach is based on the concept of scanning random locations in a field and then using the spatial coordinates and logVOA of the tested locations to predict the VOA of untested ones. A leave-one-out cross validation (LOOCV) technique [44] was used to partition the data into two subsets, namely, samples of sizes 330 and 50, which were used for training and testing, respectively. The results suggest that VOA can be effectively predicted using the model described by Equation (12). The prediction accuracy presented in Figure S2) is  $r \sim 0.8$  (a positive high Pearson correlation). Being able to predict VOA helps to minimize time spent on GPR field scanning. Thus, both predicted and observed VOA can be combined to create a plot error structure.

## 4. Discussion

The non-invasive prediction or estimation of fyld in cassava plantations is important since bulked roots raise this plant's economic value as food and income. To the plant breeder, fyld is a valued trait to ensure in the products provided to farmers. For many years, there was no effective method by which to determine the rate of root formation



except time-consuming and laborious excavation. Recently, GPR has become an enabling technology with which to overcome this gap. The application of GPR is especially important in breeding during early-stage testing when large numbers of genotypes are screened in unreplicated plots.

Spatial variability, which can be quantified using a GPR diagnostic attribute such as VOA, is well known in the agricultural space as it is one of the major factors that can mask the true yield-producing capability of the genotype.

Many processes concerning below-ground plant performance are not fully understood, such as spatial and temporal root-forming dynamics and their relation to heterogeneous environmental factors [52]. Accounting for the spatial pattern of subsurface heterogeneity becomes very important as it may be used to adjust for the estimation and/or prediction of yield. GPR can be used to investigate the below-ground characteristics of developing plants [6,7,32], but it has not been fully utilized to explore the role of spatial heterogeneity in agricultural field experiments. Our results presented herein agree with previous findings on the improvement of the prediction accuracy of yield through spatial adjustments [8]. However, most of the spatial adjustments hitherto performed were based on a simple  $AR1 \times AR1$  model. Such models are endogenous; hence, they are easier to use as their plot error structure is discerned solely from the design effects (i.e., the row and column layout of the agricultural plots).

The use of a GPR-derived plot error structure is an exogenous approach that offers a complementary measure of spatial heterogeneity. The deployment of GPR offers breeders a straightforward procedure for quantifying a field's spatial heterogeneity at different stages of a growing season. GPR is also a tool that can be used to target the onset of early maturity in a root via a proximal measurement of its biomass [6]. As shown in Figure S2, the result of spatial kriging demonstrates that a subsampling of VOA could be used to interpolate and extrapolate VOA to unsampled locations. The kriging procedure can help field technicians minimize their time spent in the field conducting GPR scans. For example, instead of scanning 500 field plots, 300 randomly selected plots could be scanned, and the application of the kriging method to the VOA results could be performed to predict the VOA on the remaining 200 plots.

The spatial autoregressive coefficient  $\rho$  estimated by the CAR model is higher than that of the SAR model. However, the AICC and Log likelihood estimates from both models, which were not significantly different, suggest they would produce an adjustment similar to yield estimation.

The  $AR1 \times AR1$  model's results compare favorably with those of the CAR model. There is only a marginal difference in the overall BLUE average standard error of the genotype. The grand difference in the MV is a result of the marginal differences in the SEs of each genotype. Since the SE is a measure of accuracy, the CAR model can be adjudged to provide better accuracy of the estimated yield at the individual level of the genotype.

The antenna orientation effect as the cart traverses rugged terrain and other types of measurement uncertainties are common in GPR [24]. Thus, the reliability of the method described in this study is subject to random and systematic errors. An important type of error is caused by complicated reflections from cassava roots in some plots, which arise as a result of irregularities in antenna orientation. To circumvent this problem, an optimal antenna orientation to create the desired offset in field plots can be achieved by burying metal test objects at specific locations along the plot row. Plot rows along which no reflection from this metal object are observed can be adjudged to contain an "offset error" as a result of a change in the angle of orientation, which is also called the "look angle". In this study, a constant visual assessment of the clamp holding the antenna was performed to ensure that the look angle did not change. Furthermore, caution must be exercised while using GPR, especially for agricultural purposes, in order to avoid the plodding of plot rows. Plodding is a term that describes walking heavily or trudging on the GPR target area of a scan. Plodding can lead to soil compaction, thus adding to the complexity of the subsurface and ultimately impairing signal penetration.

In a practical agricultural application of GPR, it is recommended to scan the experimental plot rows before the plants start to germinate. This would allow the antenna to easily hover on top of the plot row without needing to consider irregularities in antenna orientation and its associated effects, such as reflections from cassava roots, since germination has not occurred. This was not possible in this study because cassava is only commonly grown as a crop outside of the United States; thus, all the cassava plants from the field trial identified in Momil, Colombia, had already germinated.

Nonetheless, the sampling approach described herein can be considered to comprise a post-hoc dual approach whereby root biomass at the onset of root maturity (about 5 months after planting) and spatial variation can be jointly estimated. Additionally, to minimize or eliminate some of the limitations described above, there may be an advantage in utilizing two antennae operating at different frequencies during data acquisition, where one is tuned for root biomass and the other is tuned for soil heterogeneity, or in comparing the use of different multichannel antenna configurations; however, this enhancement may cause field operations to become more cumbersome.

In addition, another consideration regarding the use of GPR in plant breeding programs is the use of an efficient storage system for mapping GPR radargrams to an associated field plot. Such a mapping technique can provide additional data for retrospective analysis, thus minimizing data management complexities that may arise from complex data relationships [53].

## 5. Conclusions

This study presents the first GPR-derived spatial adjustment to yield applied to cassava and offers similar promising affordances to other root and tuber crops. The results of this study indicate a potential advancement in the utility of GPR beyond the estimation of root biomass. Exogenous approaches, such as the use of a GPR-derived proxy measure of heterogeneity, are useful methods for creating field maps of spatial variation at different times of a season and for adjusting yield estimation at harvest. Thus, the procedure detailed herein should help breeders plan field trials and select genotypes more efficiently. Interpolating and extrapolating GPR-derived VOA from scanned to unscanned plots would also help reduce time spent and resources used in the field.

**Supplementary Materials:** The following supporting information can be downloaded at: <https://www.mdpi.com/article/10.3390/rs15071771/s1>.

**Author Contributions:** Conceptualization, A.A., M.E.E. and D.B.H.; data acquisition, A.A. and H.R.-G.; software, A.A. and H.R.-G.; analysis, A.A.; writing—original draft preparation, A.A.; review and editing, M.E.E., O.A.M.-L., H.R.-G. and D.B.H.; funding acquisition, D.B.H. All authors have read and agreed to the published version of the manuscript.

**Funding:** This work was supported by the funding provided to Dirk B. Hays via the NSF-BREAD (award number 1543957) program through Texas A&M University.

**Data Availability Statement:** The data presented are available on request.

**Acknowledgments:** The authors would like to thank Xioafei Zhang and Camilo Vargas for their excellent support during data acquisition.

**Conflicts of Interest:** The authors declare no competing interests.

## References

1. Hardie, M. Review of novel and emerging proximal soil moisture sensors for use in agriculture. *Sensors* **2020**, *20*, 6934. [CrossRef]
2. Abbas, F.; Afzaal, H.; Farooque, A.A.; Tang, S. Crop yield prediction through proximal sensing and machine learning algorithms. *Agronomy* **2020**, *10*, 1046. [CrossRef]
3. Tonukari, N.J. Cassava and the future of starch. *Electron. J. Biotechnol.* **2004**, *7*, 12–15. [CrossRef]
4. Chiona, M.; Ntawuruhunga, P.; Mukuka, I.; Chalwe, A.; Phiri, N.; Chikoti, P.; Simwambana, M. *Growing Cassava: Training Manual for Extension & Farmers in Zambia*; International Institute of Tropical Agriculture (IITA): Lusaka, Zambia, 2016; pp. 1–77.

5. Teeken, B.; Olaosebikan, O.; Haleegoah, J.; Oladejo, E.; Madu, T.; Bello, A.; Parkes, E.; Egesi, C.; Kulakow, P.; Kirscht, H.; et al. Cassava Trait Preferences of Men and Women Farmers in Nigeria: Implications for Breeding. *Econ. Bot.* **2018**, *72*, 263–277. [[CrossRef](#)] [[PubMed](#)]
6. Agbona, A.; Teare, B.; Ruiz-Guzman, H.; Dobrev, I.D.; Everett, M.E.; Adams, T.; Montesinos-Lopez, O.A.; Kulakow, P.A.; Hays, D.B. Prediction of root biomass in cassava based on ground penetrating radar phenomics. *Remote Sens.* **2021**, *13*, 4908. [[CrossRef](#)]
7. Delgado, A.; Hays, D.B.; Bruton, R.K.; Ceballos, H.; Novo, A.; Boi, E.; Selvaraj, M.G. Ground penetrating radar: A case study for estimating root bulking rate in cassava (*Manihot esculenta* Crantz). *Plant Methods* **2017**, *13*, 65. [[CrossRef](#)]
8. Elias, A.A.; Rabbi, I.; Kulakow, P.; Jannink, J.L. Improving genomic prediction in cassava field experiments using spatial analysis. *G3 Genes Genomes Genet.* **2018**, *8*, 53–62. [[CrossRef](#)] [[PubMed](#)]
9. Papadakis, J. Méthode statistique pour des expériences sur champ. *Bull. Inst. Amél. Plantes Salonique* **1937**, *30*, 23.
10. Lill, W.J.; Gleeson, A.C.; Cullis, B.R. Relative accuracy of a neighbour method for field trials. *J. Agric. Sci.* **1988**, *111*, 339–346. [[CrossRef](#)]
11. Cullis, B.R.; Gleeson, A.C. Spatial Analysis of Field Experiments—An Extension to Two Dimensions. *Biometrics* **1991**, *47*, 1449–1460. [[CrossRef](#)]
12. Gilmour, A.R.; Cullis, B.R.; Verbyla, A.P. Accounting for Natural and Extraneous Variation in the Analysis of Field Experiments. *J. Agric. Biol. Environ. Stat.* **1997**, *2*, 269–293. [[CrossRef](#)]
13. Radočaj, D.; Jug, I.; Vukadinović, V.; Jurišić, M.; Gašparović, M. The effect of soil sampling density and spatial autocorrelation on interpolation accuracy of chemical soil properties in arable cropland. *Agronomy* **2021**, *11*, 2430. [[CrossRef](#)]
14. Canal Filho, R.; Molin, J.P. Spatial distribution as a key factor for evaluation of soil attributes prediction at field level using online near-infrared spectroscopy. *Front. Soil Sci.* **2022**, *2*, 984963. [[CrossRef](#)]
15. Shit, P.K.; Bhunia, G.S.; Maiti, R. Spatial analysis of soil properties using GIS based geostatistics models. *Model. Earth Syst. Environ.* **2016**, *2*, 107. [[CrossRef](#)]
16. Kiani, M.; Hernandez-ramirez, G.; Quideau, S.A.M. Spatial variation of soil quality indicators as a function of land use and topography. *Can. J. Soil Sci.* **2020**, *100*, 463–478. [[CrossRef](#)]
17. Negassa, W.; Baum, C.; Schlichting, A.; Müller, J.; Leinweber, P. Small-scale spatial variability of soil chemical and biochemical properties in a rewetted degraded Peatland. *Front. Environ. Sci.* **2019**, *7*, 116. [[CrossRef](#)]
18. Corwin, D.L.; Lesch, S.M. Characterizing soil spatial variability with apparent soil electrical conductivity: I. Survey protocols. *Comput. Electron. Agric.* **2005**, *46*, 103–133. [[CrossRef](#)]
19. Li, S.L.; Liang, W.L. Spatial-temporal soil water dynamics beneath a tree monitored by tensiometer-time domain reflectometry probes. *Water* **2019**, *11*, 1662. [[CrossRef](#)]
20. Huisman, J.A.; Snepvangers, J.J.J.C.; Bouten, W.; Heuvelink, G.B.M. Mapping spatial variation in surface soil water content: Comparison of ground-penetrating radar and time domain reflectometry. *J. Hydrol.* **2002**, *269*, 194–207. [[CrossRef](#)]
21. Weihermüller, L.; Huisman, J.A.; Lambot, S.; Herbst, M.; Vereecken, H. Mapping the spatial variation of soil water content at the field scale with different ground penetrating radar techniques. *J. Hydrol.* **2007**, *340*, 205–216. [[CrossRef](#)]
22. Campos, J.R.d.R.; Vidal-Torrado, P.; Modolo, A.J. Use of Ground Penetrating Radar to study spatial variability and soil stratigraphy. *Eng. Agric.* **2019**, *39*, 358–364. [[CrossRef](#)]
23. Wollschläger, U.; Gerhards, H.; Yu, Q.; Roth, K. Multi-channel ground-penetrating radar to explore spatial variations in thaw depth and moisture content in the active layer of a permafrost site. *Cryosphere* **2010**, *4*, 269–283. [[CrossRef](#)]
24. Redman, D.; Galagedara, L.; Parkin, G. Measuring Soil Water Content with the Ground Penetrating Radar Surface Reflectivity Method: Effects of Spatial Variability. In *2003 ASAE Annual Meeting*; American Society of Agricultural and Biological Engineers: St. Joseph, MI, USA, 2013; p. 0300. [[CrossRef](#)]
25. De Benedetto, D.; Barca, E.; Castellini, M.; Popolizio, S.; Lacolla, G.; Stellacci, A.M. Prediction of Soil Organic Carbon at Field Scale by Regression Kriging and Multivariate Adaptive Regression Splines Using Geophysical Covariates. *Land* **2022**, *11*, 381. [[CrossRef](#)]
26. Fedorova, L.L.; Sokolov, K.O.; Savvin, D.V.; Kulyandin, G.A. Analysis of Variance Amplitudes of Signals for Detecting Structural Permafrost Heterogeneities by Ground Penetrating Radar. In *Proceedings of the 15th International Conference on Ground Penetrating Radar*, Brussels, Belgium, 30 June–4 July 2014; pp. 301–304.
27. Solla, M.; Lagüela, S.; Riveiro, B.; Lorenzo, H. Non-destructive testing for the analysis of moisture in the masonry arch bridge of Lubians (Spain). *Struct. Control Health Monit.* **2013**, *20*, 1366–1376. [[CrossRef](#)]
28. Rasol, M.A.; Pérez-Gracia, V.; Fernandes, F.M.; Pais, J.C.; Santos-Assunção, S.; Santos, C.; Sossa, V. GPR laboratory tests and numerical models to characterize cracks in cement concrete specimens, exemplifying damage in rigid pavement. *Meas. J. Int. Meas. Confed.* **2020**, *158*, 107662. [[CrossRef](#)]
29. Annan, A.P. GPR—History, Trends, and Future Developments. *Subsurf. Sens. Technol. Appl.* **2002**, *3*, 253–270. [[CrossRef](#)]
30. Turpin, N.; Stapleton, L.; Perret, E.; Van Der Heide, C.M.; Garrod, G.; Brouwer, F.; Voltr, V.; Cairol, D. Assessment of multifunctionality and jointness of production. In *Environmental and Agricultural Modelling: Integrated Approaches for Policy Impact Assessment*; Springer: Dordrecht, Netherlands, 2010; pp. 11–35, ISBN 9789048136186.
31. Zhu, S.; Huang, C.; Su, Y.; Sato, M. 3D Ground Penetrating Radar to Detect Tree Roots and Estimate Root Biomass in the Field. *Remote Sens.* **2014**, *6*, 5754–5773. [[CrossRef](#)]

32. Dobreva, I.D.; Ruiz-Guzman, H.A.; Barrios-Perez, I.; Adams, T.; Teare, B.L.; Payton, P.; Everett, M.E.; Burow, M.D.; Hays, D.B. Thresholding Analysis and Feature Extraction from 3D Ground Penetrating Radar Data for Noninvasive Assessment of Peanut Yield. *Remote Sens.* **2021**, *13*, 1896. [CrossRef]
33. Butnor, J.R.; Doolittle, J.A.; Kress, L.; Cohen, S.; Johnsen, K.H. Use of ground-penetrating radar to study tree roots in the southeastern United States. *Tree Physiol.* **2001**, *21*, 1269–1278. [CrossRef]
34. Liu, X.; Dong, X.; Xue, Q.; Leskovar, D.I.; Jifon, J.; Butnor, J.R.; Marek, T. Ground penetrating radar (GPR) detects fine roots of agricultural crops in the field. *Plant Soil* **2018**, *423*, 517–531. [CrossRef]
35. Jol, H.M. *Ground Penetrating Radar Theory and Applications*, 1st ed.; Elsevier: Oxford, UK, 2009; ISBN 9780080951843.
36. Everett, M.E. *Near-Surface Applied Geophysics*; Cambridge University Press: New York, NY, USA, 2013; ISBN 978-1-107-01877-8.
37. Kim, K.; Scott, W.R. Design of a resistively loaded vee dipole for ultrawide-band ground-penetrating radar applications. *IEEE Trans. Antennas Propag.* **2005**, *53*, 2525–2532.
38. Nuzzo, L.; Alli, G.; Guidi, R.; Cortesi, N.; Sarri, A.; Manacorda, G.; Ingegneria, I.D.S.; Sistemi, D. A new densely-sampled Ground Penetrating Radar array for landmine detection. In Proceedings of the 15th International Conference on Ground Penetrating Radar, Brussels, Belgium, 30 June–4 July 2014; pp. 969–974.
39. Cropphenomics. Crop Phenomics LLC, College Station, TX, USA. Available online: <https://cropphenomics.com> (accessed on 18 January 2023).
40. Topp, G.C.; Davis, J.L.; Annan, A.P. Electromagnetic determination of soil water content: Measurements in coaxial transmission lines. *Water Resour. Res.* **1980**, *16*, 574–582. [CrossRef]
41. Tsai, P.J.; Lin, M.L.; Chu, C.M.; Perng, C.H. Spatial autocorrelation analysis of health care hotspots in Taiwan in 2006. *BMC Public Health* **2009**, *9*, 464. [CrossRef]
42. Bivand, R.S.; Wong, D.W.S. Comparing implementations of global and local indicators of spatial association. *Test* **2018**, *27*, 716–748. [CrossRef]
43. Paula, M. Geospatial Health Data: Modelling and Visualization with R-INLA and Shiny. Available online: <https://www.paulamoraga.com/book-geospatial/sec-arealdatatheory.html> (accessed on 10 January 2023).
44. Montesinos López, O.A.; Montesinos López, A.; Crossa, J. *Multivariate Statistical Machine Learning Methods for Genomic Prediction*; Springer Nature: Berlin, Germany, 2022; ISBN 9783030890094.
45. Pinheiro, J.; Bates, D.; R Core Team. nlme: Linear and Nonlinear Mixed Effects Models. Available online: <https://cran.r-project.org/package=nlme> (accessed on 10 December 2022).
46. Rodríguez, L.S.; Muñoz, F. *breedR: Statistical Methods for Forest Genetic Resources Analysts*. In *IUFRO Genomics and Forest Tree Genetics*; Hindustan Aeronautics Limited: Arcachon, France, 2016.
47. Simpson, T.W. *Comparison of Response Surface and Kriging Models in the Multidisciplinary Design of an Aerospike Nozzle*; NASA ICASE Rep.; NASA: Washington, DC, USA, 1998.
48. Finley, A.O.; Banerjee, S.; Carlin, B.P. spBayes: An R Package for Univariate and Multivariate Hierarchical Point-referenced Spatial Models. *J. Stat. Softw.* **2007**, *19*, 1–24. [CrossRef] [PubMed]
49. R Core Team. *R: A Language and Environment for Statistical Computing*; R Foundation for Statistical Computing: Vienna, Austria, 2014.
50. Sugiura, N. Further Analysis of the Data by Anaike’s Information Criterion and the Finite Corrections. *Commun. Stat. Theory Methods* **1978**, *7*, 13–26. [CrossRef]
51. Shekhar, S.; Xiong, H. Encyclopedia of GIS. Available online: [https://books.google.com/books?id=6q2lOfLnwkAC&printsec=frontcover&source=gbs\\_ge\\_summary\\_r&cad=0#v=onepage&q&f=false](https://books.google.com/books?id=6q2lOfLnwkAC&printsec=frontcover&source=gbs_ge_summary_r&cad=0#v=onepage&q&f=false) (accessed on 13 February 2023).
52. Metzner, R.; van Dusschoten, D.; Bühler, J.; Schurr, U.; Jahnke, S. Belowground plant development measured with magnetic resonance imaging (MRI): Exploiting the potential for non-invasive trait quantification using sugar beet as a proxy. *Front. Plant Sci.* **2014**, *5*, 469. [CrossRef]
53. Agbona, A.; Peteti, P.; Teeken, B.; Olaosebikan, O.; Bello, A.; Parkes, E.; Rabbi, I.; Mueller, L.; Egesi, C.; Kulakow, P. Data Management in Multi-disciplinary African RTB Crop Breeding Programs. In *Towards Responsible Plant Data Linkage: Data Challenges for Agricultural Research and Development*; Williamson, H.F., Leonelli, S., Eds.; Springer: Cham, Switzerland, 2022; p. 19, ISBN 978-3-031-13275-9.

**Disclaimer/Publisher’s Note:** The statements, opinions and data contained in all publications are solely those of the individual author(s) and contributor(s) and not of MDPI and/or the editor(s). MDPI and/or the editor(s) disclaim responsibility for any injury to people or property resulting from any ideas, methods, instructions or products referred to in the content.